Soft Matter

Accepted Manuscript

This is an *Accepted Manuscript*, which has been through the Royal Society of Chemistry peer review process and has been accepted for publication.

Accepted Manuscripts are published online shortly after acceptance, before technical editing, formatting and proof reading. Using this free service, authors can make their results available to the community, in citable form, before we publish the edited article. We will replace this *Accepted Manuscript* with the edited and formatted *Advance Article* as soon as it is available.

You can find more information about *Accepted Manuscripts* in the Information for Authors.

Please note that technical editing may introduce minor changes to the text and/or graphics, which may alter content. The journal's standard Terms & Conditions and the Ethical guidelines still apply. In no event shall the Royal Society of Chemistry be held responsible for any errors or omissions in this *Accepted Manuscript* or any consequences arising from the use of any information it contains.

ROYAL SOCIETY OF CHEMISTRY

www.rsc.org/softmatter

Journal Name

ARTICLE TYPE

Cite this: DOI: 10.1039/xxxxxxxxxx

Investigation of the dynamics of growth of polymer materials obtained by combined pervaporation and micro-moulding†

Cédric Laval,[a] Philippe Poulin,[b‡] and Jean-Baptiste Salmon*[a]

Received Date
Accepted Date

DOI: 10.1039/xxxxxxxxxx

www.rsc.org/journalname

We report an extensive study of the concentration process of aqueous polymer solutions confined within microfluidic channels, owing to the pervaporation of water through the matrix of the chip. Concentration of polymer continuously increases up to the formation of a dense material which eventually invades the channel. This technology can be used to fabricate micro-composites of different shapes starting from dilute inks. We use both theory and screening experiments to show that the dynamics of growth can be predicted by simple conservation equations. More precisely, we establish a quantitative prediction of the growth dynamics taking into account deformations of the soft channels of the moulds, and the solvent chemical activity of the polymer solution. The present results based on general transport equations for binary mixtures provide direct guidance for the design of micro-fabricated materials considering their shape, dimensions, time scale of fabrication, and chemical composition. This quantitative framework is indeed essential to engineer integrated polymer-based micro-devices by using combined pervaporation and microfluidic moulding.

1 Introduction

Microfluidic *pervaporation* is an efficient and versatile technique to make micro-scaled structures (typical dimensions $10 \times 10\ \mu\text{m}^2 \times 1$ cm), starting from dilute solutions or colloidal dispersions[1–5]. This procedure makes use of a dead-end channel embedded in a poly(dimethylsiloxane) (PDMS) membrane and connected to a reservoir containing a dilute dispersion, see Figure 1. *Pervaporation* of water through the PDMS matrix (at a rate q_e per unit length, see inset of Figure 1a), drives a flow from the reservoir up to the channel tip at a flow rate $\sim L_0 q_e$ (~ 10 nL/hr for $L_0 \sim 10$ mm and $q_e \sim 1\ \mu\text{m}^2/\text{s}$). This flow in turn enriches *continuously* the tip of the channel with solutes or particles, up to the formation of a solid which eventually invades the channel, see Figure 1b. This technique thus combines both *micro-moulding* imparted by the microfluidic mold, and *concentration* by pervaporation to obtain micro-scaled materials from dilute solutions or suspensions. Note that this tool also makes possible the *dynamic* exploration of the phase diagram of a complex fluid, from a dilute mixture up to a solid, and it was used for such a purpose on various *soft matter* systems (surfactants, copolymers, inorganic salts, colloidal dispersions...)[6–9]

Conventional microfabrication techniques, including micro moulding in capillaries, photolithography or 3D printing, generally require the need for UV- or heat- curable prepolymers or thermoplastics[10–14]. By contrast, microfluidic pervaporation allows the use of almost any type of materials from colloids[1–5] to polymer solutions[15,16]. Nevertheless, microfluidic pervaporation, in spite of its superior versatility and high spatial resolution, still suffers from severe limitations and in particular from a lack of predictable fabrication time scales. The latter depend on the dynamics of material concentration as time elapses. In the present work, we theoretically and experimentally elucidate the mechanisms of concentration of dilute polymer solutions up to the growth of micro-materials within the channels. We show

[a] CNRS, Solvay, LOF, UMR 5258, Univ. Bordeaux, F-33600 Pessac, France. E-mail: jean-baptiste.salmon-exterieur@solvay.com
[b] Centre de Recherche Paul Pascal, Avenue Schweitzer, 33600 Pessac, France.
† Electronic Supplementary Information (ESI) available: Details concerning the numerical resolution of eqs 3 and 4. Experimental details on the fabrication protocols. Closer view of the solidification front. See DOI: 10.1039/b000000x/

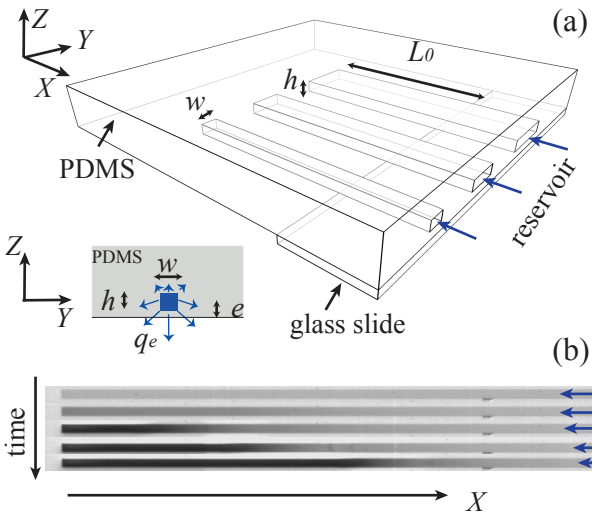

Fig. 1 (a) Shematic views of parallel *micro-pervaporators* embedded in a PDMS mold sealed by a PDMS membrane of thickness e (typical dimensions $h = 25$, $w = 100$, $e = 25$ μm, and $L_0 = 10$ mm). Blue arrows indicate the pervaporation-induced flow. Inset: transverse view, q_e is the pervaporation rate through the PDMS matrix (per unit length). (b) Growth of a composite material inside the channel . Blue arrows indicate the incoming pervaporation-induced flux ($w = 150$ μm). This experimental case corresponds to the growth of a composite PVA/CNT material, see text.

that the key ingredients of both the concentration of the solution and of the material growth are captured by basic modeling using transport equations.

Experimentally, we study aqueous solutions of poly(vinyl alcohol) (PVA), in which we dispersed a small amount of carbon nanotubes (CNT) to get estimates of the concentration fields within the channels during the process. We first show using microfluidic screening experiments that the dynamics of concentration and growth of such materials is governed by the geometry of the channel and the polymer concentration in the dilute dispersion. We also show using local measurements of the CNT concentration within the channel that a model taking into account the non-ideality of the polymer solution is able to account *semi-quantitatively* for the observed dynamics. We also report significant deflections of the PDMS matrix during the solidification leading thus to materials with a transverse cross-section smaller than the one imparted by the PDMS mold. We finally show that a simplified model taking into account these deflections can predict quantitatively the growth of the materials.

Beyond our extensive investigation of the dynamics of concentration, we demonstrate that the micro-pervaporation technique makes possible the fabrication of PVA/CNT *composites* with controlled shapes, see Figure 1b. These materials can be extracted from the PDMS matrix which serves as a mold along with being at the core of pervaporation process. Complex shapes can even be obtained, see the scanning electron microscopy (SEM) images displayed in Figure 2, either by manual handling of planar structures made in networks of microfluidic channels, or directly using two-level microfluidic molds obtained using standard alignments processes. This technique opens the way for the design of original materials which may have potential applications in the field of organic Micro-Electro-Mechanical Systems (MEMS) [17,18]. We will report in a separate paper a detailed investigation of the electrical properties of the PVA/CNT micro-composites obtained by this technique, and their possible use as functional building blocks for MEMS.

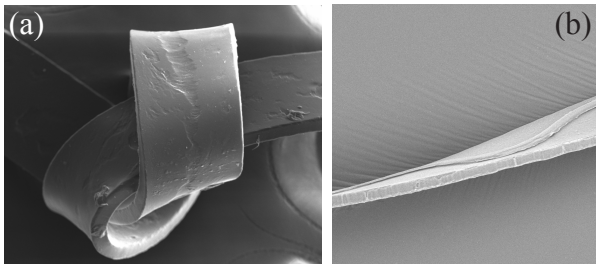

Fig. 2 SEM pictures of composite PVA/CNT materials with complex shapes. (a) The knot was *laced* manually from a planar beam of thickness 25 and width 150 μm. (b) This shape was molded directly in a two-level micro-channel (thickness of the beam 25 μm and of the superimposed curved structure 10 μm).

Our article is organized as follows. We first briefly present the basic functioning of micro-pervaporation and we present in details the theoretical description for a binary mixture such as PVA in water. We then present experimental details and the complex fluid under study in section 3. We then report in section 4 our experimental investigation of the concentration process of such solutions within the channel, up to the growth of a material. We finally compare these results with our theoretical description based on transport equations, up to obtain a quantitative agreement when deformations of the PDMS matrix are taken into account.

Our results provide a general framework concerning the dynamics of growth of polymer micro-scaled materials regarding the channel geometry, the initial concentrations of the solutions, and the pervaporation rates. Such a quantitative prediction of the time scales needed from micro-fabricating polymer materials is essential to design polymer components up to integrated micro-devices using combined micromoulding and pervaporation.

2 Theoretical description of the microfluidic pervaporation of polymer solutions

In the present section, we present both the functioning of micro-pervaporators and the theoretical description of the *expected* concentration dynamics for a binary mixture. We then apply this model to the case of a polymer solution, and we derive a simplified model which captures the key ingredients of the expected dynamics of concentration and growth of polymer materials.

2.1 Basics of microfluidic pervaporation

The general description of the functioning of micro-pervaporation can be found in refs[19] (and in refs.[6–9] for specific systems), and we give below only some key ingredients for the case of a binary mixture. The basic functioning is sketched in Figure 1a: the typical dimensions of the channels investigated in the present work are $h \times w = 25 \times 100\ \mu\text{m}^2$ and the channels are embedded in a PDMS block (≈ 5 mm thick) sealed by a thin PDMS membrane of thickness $e \approx 25\ \mu$m. For such a linear geometry, pervaporation of water mainly occurs through the membrane at a rate q_e per unit length of the order of 2–3 μm^2/s (see inset of Figure 1a, q_e is defined here for a vanishing external humidity h_e). Pervaporation of pure water along the channel length L_0 drives a flow from the reservoir at a rate $q_e L_0$ of the order of 10 nL/hr for the cases investigated in the present work ($L_0 \approx 10$ mm).

We now consider the case of a binary aqueous solution, such as PVA in water, with ϕ the solute volume fraction. For homogeneous concentrations over the transverse dimensions of the channel (i.e. for $q_e < D$ with D the typical interdiffusion coefficient of the solution[19]), Schindler and Ajdari derived a 1D model based on classical transport equations, which describes the dynamics of concentration within the channel[19]. Pervaporation drives a flow which follows mass conservation

$$(hw)\partial_X V = -(a(\phi) - h_e) q_e\,, \tag{1}$$

where $V(X)$ is the mean velocity within the channel and $a(\phi)$ the local chemical activity of water (the origin of the X axis is set at the tip of the channel). The term $a(\phi) - h_e$ thus represents the *driving force* of pervaporation through the membrane. This pervaporation-induced flow in turn drives the solutes from the reservoir toward the tip of the channel where they accumulate. The temporal evolution of the solute concentration along the channel follows the conservation equation

$$\partial_T \phi + \partial_X(\phi V(X) - D(\phi)\partial_X \phi) = 0\,, \tag{2}$$

with $D(\phi)$ the collective diffusion coefficient of the solution (in the reference frame of the volume-averaged velocity)[19].

With the unitless dimensions $x = X/L_0$, $t = T/\tau_e$ and $v = V/(L_0/\tau_e)$ with $\tau_e = hw/q_e$, this model now reads

$$\partial_x v = -(a(\phi) - h_e)\,, \tag{3}$$

$$\partial_t \phi + \partial_x(\phi v - \frac{\hat{D}(\phi)}{\text{Pe}}\partial_x \phi) = 0\,, \tag{4}$$

with the Péclet number $\text{Pe} = L_0^2/(D_0\tau_e)$, and $D = D_0\hat{D}(\phi)$ with D_0 the value of the collective diffusion coefficient in the limit $\phi \to 0$ ($\hat{D}(\phi \to 0) = 1$), thus corresponding to the self-diffusion coefficient of the polymer in the dilute regime[20].

The dynamics of the solute concentration can be predicted using the numerical integration of eqs 3 and 4 with appropriate boundary conditions and the knowledge of both $a(\phi)$ and $D(\phi)$.

2.2 Numerical resolution for PVA/water binary mixtures

To get quantitative values of the concentration process for the PVA solutions studied in our work, we solved eqs 3 and 4 using the chemical activity described by the following Flory-Huggins model

$$a(\phi) = (1-\phi)\exp(\phi + \chi\phi^2) \tag{5}$$

with $\chi(\phi) = 5.934 - 5.4556(1-\phi)^{0.0725}$, see Figure 3a. These values were measured by Jeck *et al.* who investigated the dynamics of water sorption into PVA membranes[21]. As shown later, the precise shape of the curve $a(\phi)$ is not critical to capture the dynamics of the concentration of PVA within the channel. For the sake of simplicity without the loss of generality, we also assumed $h_e = 0$.

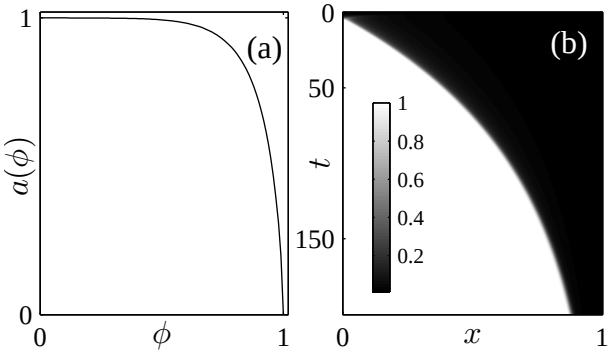

Fig. 3 (a) Theoretical activity of the polymer solution according to eq 5[21]. (b) Space-time plot of the concentration field $\phi(x,t)$ calculated for $\text{Pe} = 10^4$ and $\phi_0 = 0.01$. Concentrations are coded using a gray scale shown in inset.

In the range covered by our experiments (see later in section 3), $L_0 = 5$–15 mm, $\tau_e = 200$–1200 s, and $D_0 \approx 10^{-11}$ m^2/s (a rough estimate using the Stokes-Einstein relation and radius of gyration 15–20 nm[22]). Péclet numbers thus range from 10^3 to 10^5 indicating that the convective transport dominates the process, and we

will thus assume $\hat{D} = 1$ for simplicity. All the details concerning the numerical resolution of eqs 3 and 4 are given in SI.

Figure 3b reports a typical space-time plot of the concentration profile $\phi(x,t)$ calculated for $\mathrm{Pe} = 10^4$ and $\phi_0 = 0.01$ (concentrations are coded using a gray scale). After a transient time $\tau_n \approx 5$, a dense state ($\phi = 1$) invades the channel at a rate which significantly slows down. Figure 4 displays both the calculated velocity profiles and concentration fields at different specific times to better evidence the dynamics before and after τ_n.

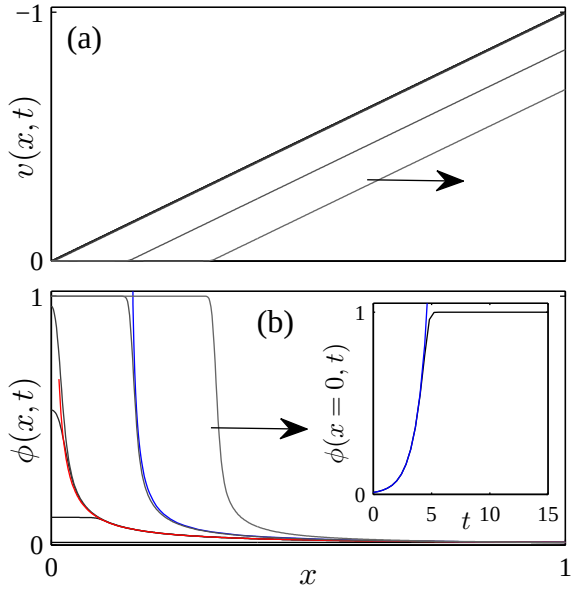

Fig. 4 (a) Velocity $v(x,t)$, and (b) concentration profiles $\phi(x,t)$ vs. x for $t = 0$, 2.4, 4, 4.8, 19.6 and 39.7 calculated for $\mathrm{Pe} = 10^4$ and $\phi_0 = 0.01$ (from black to gray lines). The two arrows indicate the growth of the dense material in the channel. (b) The red curve corresponds to $\phi = \phi_0/x$. For $t = 19.6$, the blue curve corresponds to the shifted hyperbolic profile given by eq 7. Inset: Concentration at the tip vs. t. The blue curve is $\phi = \phi_0 \exp(t)$.

For $t < \tau_n$, all the velocity profiles collapse on the single linear profile $v(x) = -x$, as for the case of a dilute solution ($a(\phi) \approx 1$, see eq 3). The increase of the concentration towards $\phi \to 1$ at $x \to 0$ only decreases the chemical activity at the tip of the channel but does not modify significantly $v(x)$ along the channel. As the transport is mainly dominated by convection ($\mathrm{Pe} \gg 1$), we already derived analytical approximations in ref[4] for the concentration fields:

$$\phi = \phi_0 \exp(t) \quad \text{for } t < -\log(\phi_0 x),$$
$$\phi = \phi_0/x \quad \text{either}. \tag{6}$$

The concentration increases exponentially along the channel until it reaches the steady *hyperbolic* profile $\phi = \phi_0/x$. This peculiar shape corresponds to a constant flux dominated by convection, i.e. $\phi(x)v(x) = \phi_0 v(x=1) = -\phi_0$. These approximations fit correctly the concentration fields in the regime $t < \tau_n$, see Figure 4b.

At later time scales, the concentration reaches ≈ 1 at the tip, and pervaporation across the membrane vanishes as $a(\phi \to 1) \to 0$, see eq 3. In this regime, velocities are thus almost null within the dry material $\phi \approx 1$, and the latter invades the channel. We can estimate the position of the advancing front x_f of the material using the extrapolation of the velocity profile to the value 0. Upstream the front x_f, the velocity profiles are almost linear (because $a(\phi) \approx 1$ for $x > x_f$), and thus with the same slope as above, i.e. $v(x) = -(x - x_f)$.

In the *liquid* region for $x > x_f$, the transport is still dominated by convection ($\mathrm{Pe} \gg 1$), and thus $\phi(x)v(x) \approx \phi_0 v(x=1)$. Concentration profiles for $x > x_f$ are thus well-fitted by the *shifted* hyperbolic profile

$$\phi(x,t) = \phi_0 \frac{1 - x_f}{x - x_f}, \tag{7}$$

see e.g. the blue curve for $t = 19.6$.

Diffusive effects play a role only on a scale $1/\sqrt{\mathrm{Pe}}$ within the channel as expected from a scaling analysis of eqs 3 and 4[19]. We thus expect that diffusion smoothes the concentration profiles upstream x_f on a scale $1/\sqrt{\mathrm{Pe}} \approx 0.01$ in the case shown Figure 4. Fine details corresponding to the exact shape of $\hat{D}(\phi)$ are thus only contained within this small zone. We performed numerical simulations on a wide range of Péclet numbers (from 10^2 to 10^5, data not shown) and we indeed observed that the width of the profile upstream the front up to the collapse on the hyperbolic profile scales as $1/\sqrt{\mathrm{Pe}}$.

Figure 5a finally reports the front position x_f vs. t. The growth

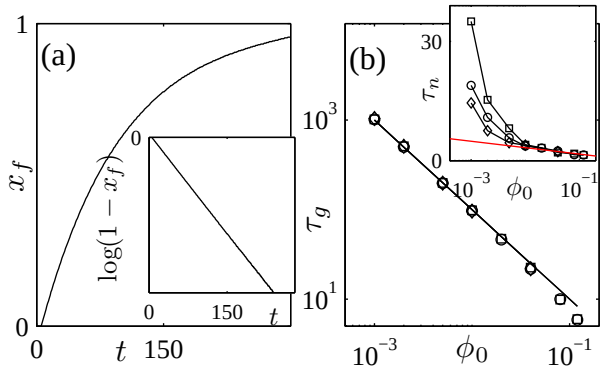

Fig. 5 (a) Front position x_f vs. t for $\mathrm{Pe} = 10^3$, $\phi_0 = 0.01$. Inset: log-lin representation. Inset: τ_n vs. ϕ_0 for the same set of Pe. Red curve: $\tau_n = -0.7\log(\phi_0)$.

rate significanly slows down and follows the exponential decay

given by

$$x_f = 1 - \exp\left(-\frac{t-\tau_n}{\tau_g}\right) \quad (8)$$

with two free parameters τ_g and τ_n which correspond respectively to the *induction* time of the material within the channel, and a typical time scale for its growth.

Figure 5b shows the values of τ_g and τ_n calculated theoretically for a wide range of ϕ_0 and for several Pe. We observed for all Pe, that $\tau_g = 1/\phi_0$, except a slight deviation for $\phi_0 > 0.05$ that we will comment below. Concerning the induction times, we observed two regimes: (i) for $\phi_0 > 0.01$, τ_n does not depend on the Péclet number and evolves logarithmically with ϕ_0; (ii) for smaller concentrations, τ_n increases importantly with the decreasing ϕ_0 and this behavior depends on Pe.

2.3 A simplified model

In the transient regime, before concentrations reach almost one at the tip of the channel, our numerical results indicate that we can safely use eq 6 corresponding to a convection-dominated transport with $v(x) \approx -x$. The concentration at the tip thus increases exponentially $\phi \approx \phi_0 \exp(t)$ independently on Pe. This regime is valid up to a critical time scale $\tau^\star = 0.5\log(\mathrm{Pe})$ where diffusion cannot be neglected anymore as the concentration gradient increases continuously at the tip[19]. Two regimes are then expected. For $\phi_0\sqrt{\mathrm{Pe}} > 1$, the concentration at the tip reaches $\phi \approx 1$ before $\tau^\star$ and induction times are thus given by $\phi_0 \exp(\tau_n) \approx 1$. This is consistent with the regime observed for $\phi_0 > 0.01$, see the logarithmic fit $\tau_n \sim -\log(\phi_0)$ shown Figure 5b. For $\phi_0\sqrt{\mathrm{Pe}} < 1$, the concentration at the tip does not reach 1 for $t \approx t^\star$, and the concentration still increases at the tip of the channel but at a rate which scales as $\phi_0\sqrt{\mathrm{Pe}}$[19]. This is the origin for the two regimes observed theoretically for τ_n see Figure 5b, with a cross-over around $\phi_0 \approx 0.01$ for the investigated range of Pe.

During the growth of the material, the incoming velocity within the channel decreases and is roughly given by $v(x=1,t) = -(1-x_f)$, see Figure 4a. Assuming that the incoming flux of solutes is convected up to the material leads to the approximate conservation equation:

$$\dot{x}_f \approx -\phi_0(1-x_f)\,. \quad (9)$$

The integration of this last relation leads to the exponential decay of the growth rate, see eq 8, with $\tau_g = 1/\phi_0$. This is indeed the behavior observed theoretically, see Figure 5b. The exponential slowing down thus corresponds to the decrease of the *effective length* of pervaporation during the growth of the material. The latter does not indeed contribute to pervaporation as $a(\phi) = 0$ for $\phi \approx 1$. Note that the slight deviation from the theoretical scaling $\tau_g = 1/\phi_0$ at high ϕ_0, see Figure 5b, comes from the fact that we neglect in the conservation equation 9 the temporal variation of the concentration profile upstream the front which becomes significant only at high ϕ_0.

3 Materials and methods

3.1 Dispersions investigated

We investigated dispersions of CNT in PVA solutions which were already investigated in depth for their ability to form composite materials using various processes[23,24]. PVA is a semi-crystalline polymer that has a glass temperature transition of about 80°C when fully dry[25,26]. However, this temperature transition strongly decreases in presence of minute amounts of water[25,26]. The visco-elastic coefficients of the glassy and rubbery states vary by orders of magnitude at the glass transition. The storage modulus of dry PVA in its glassy state is of a few GPa[26], well above the modulus of the PDMS matrix of a few MPa.

We initially prepared a stock aqueous solution of PVA (72 kg/mol, Sigma-Aldrich) in deionized water at a mass fraction 7.5%. To fully solubilize PVA, we first heated the solution at 90°C for 1 hr and left it to cool to room temperature for ≈ 12 hr. The PVA volume fraction of this solution $\phi_0 \approx 0.06$ is estimated from the PVA density (1.27 g/cm^3) and assuming the additivity of the volumes. We also prepared a 10 g stock dispersion of CNT in water by sonicating 90 mg of multi-walled CNT (Arkema, GraphiStrength C100) in the presence of 120 mg of a polyoxyethylene glycol alkyl ether surfactant (Brij78, Sigma-Aldrich), as already reported[27]. All the dispersions investigated later in the present work were obtained through appropriate mixing and dilutions of the two above stock solutions. Initial volume fractions of PVA are in the range $\phi_0 = 0.001$ to 0.03, whereas CNT mass fractions remains always below $\psi_0 < 5\,10^{-4}$. For all the investigated cases, the ratio of volume fractions CNT/PVA are in the range 0.0025–0.025 (assuming the density of CNT to 1.8).

The complex fluid under study, CNT dispersed in a polymer solution, differs from a simple binary mixture and may not be described by the model derived above in section 2. A full theoretical description would require extensive modifications (including collective diffusion for a multi-component system[28,29]), which go well-beyond the scope of our work. However, several features of the investigated *ink* help us to keep our simple description. First, we investigated only small ratios of concentration CNT/PVA, and CNT remains therefore always dilute. Secondly, the colloidal nature of the CNT does not affect significantly the chemical activity of water which thus remains dominated by the polymer only[30]. Finally, the CNT are *tracers* within the polymer solution owing to their low diffusivity ($\sim 10^{-11}$ m^2/s in water). For the sake of simplicity, we will however assume that diffusion still homogeneizes the CNT concentration over the transverse dimensions of the channel, leading as above to a simple 1D description.

With these assumptions, the CNT concentration ψ strictly fol-

lows the polymer concentration through $\psi = (\psi_0/\phi_0)\phi$, and the dynamics of the PVA concentration remains governed by eqs 3 and 4. The assumption of homogeneity of the CNT concentration along the tranverse direction is actually supported by the perfect agreement between the theoretical predictions and the experimental measurements provided below.

3.2 Experimental Microfluidic Pervaporation

We used classical soft photolithography techniques to fabricate the chips shown shematically in Figure 1, see also the SI for details and our previous works mainly in refs[4,8,9]. For these linear geometries, the pervaporation rate q_e depends on the channel cross-section $h \times w$, and on the membrane thickness e (of the order of 25 μm in our experiments)[2,31].

To screen different conditions of concentration using a single experiment, our microfluidic designs are composed of several parallel pervaporators connected to a unique reservoir (a simple tube punched into the PDMS matrix). In the first case, we screened the incoming flux $L_0 q_e$ using 5 parallel channels with the same transverse dimensions $h \times w = 25 \times 150$ μm^2 but with L_0 ranging from 5 to 15 mm. In the second case, we screened several pervaporation rates q_e using parallel channels with a constant L_0. For the rough screening reported Figure 9a, we used 5 channels with $L_0 = 16$ mm, $h = 25$ μm, and w ranging from 100 to 500 μm. For a finer screening, see Figures 9b and 10, we investigated 15 parallel channels with $L_0 = 5$ mm, $h = 25$ μm, and w ranging logarithmically from 10 to 300 μm. In that case, q_e ranges typically from 1 to 6 μm^2/s.

To maximize the experiments and to screen different initial concentrations, our final microfluidic chips (5×7.5 cm^2) are composed of up to 12 identical units described above, yielding possibly up to $12 \times 15 = 180$ different conditions on a single chip.

In a typical experiment, the channels are filled by gently flowing the dilute dispersion into the channels (in about 1 min). The external humidity h_e is then recorded thanks to a digital humidity sensor (Sensirion SHT2x). Typical values range between 0.2 and 0.4, and temporal variations of h_e remains below 0.03 during an experiment. The duration of a experiment ranges typically from 5 to 20 hr. The experiments reported here have been performed at room temperature ($\approx$ 20–23°C).

3.3 Optical characterizations

The dynamics of concentration was recorded using a stereomicroscope (Olympus) coupled to a CCD camera (ORCA-05G, 12 bit digital output, Hamamatsu) at a low frame rate (typically 1 image/min). This setup provides images of the whole set of parallel channels described above with a typical resolution down to 3 μm per pixel. Each movie thus makes possible the screening of either different L_0 or different w in a single experiment. Typical snapshots zooming on one channel are shown in Figure 1b. The concentration process is clearly evidenced owing to the strong absorbance of CNT leading to grayscale profiles. To estimate the CNT concentration within the channel, we defined the absorbance profile $A(X)$ by

$$A(X) = -\log_{10}\left(\frac{I(X) - I_d}{I_r(X) - I_d}\right), \qquad (10)$$

where $I(X)$ is the grayscale profile along the channel, $I_r(X)$ a reference profile, and I_d the dark value of the CCD camera. As in the classical definition of absorbance, $I_r(X)$ should correspond to the profile measured using the PVA solution within the channel. However, to account for temporal variations of the illumination field during the experiments, $I_r(X)$ is defined as the grayscale profile measured at a location just outside the channel, within the PDMS matrix. This is valid as the PVA solutions do not absorb in our experimental range and this definition also correctly accounts for the spatial inhomogeneity of the illumination.

The previous relation mimics the classical definition of the absorbance with however some differences. The steromicroscope (including the illumination and collection optics) does neither illuminate strictly the sample with a parallel beam nor collect only the transmitted light. Moreover, the sample is illuminated by a halogen lamp without any filters, and the transmitted light is collected by the CCD camera on a large spectral range. However, we are confident in estimating the local concentration of CNT thanks to eq 10, as (i) the numerical aperture of the collection of our stereomicroscope is very small (NA = 0.11), and (ii) the spectral range of the absorbance of the CNT is particularly wide as compared to the spectral range delivered by an halogen lamp[32]. More importantly, the experimental measurements presented below are in excellent agreement with the theoretical predictions, demonstrating that eq. 10 yields correct estimates of the CNT concentration.

However, absorbance values saturates at $A \approx 0.8$ for high concentrations of CNT, preventing us to cover a wide range of concentrations. In our experimental configuration, the pixel values of the reference profile I_r range between 2000 and 3000 and the dark value of the CCD camera is $I_d \approx 200$. The value of saturation $A \approx 0.8$ thus corresponds to pixel intensities of $I \approx (1\text{–}2) I_d$ close to the limit of the dynamic range of the CCD in our configuration.

3.4 SEM characterizations

To acquire SEM images of the final material as shown in Figure 2, we first peeled off carefully the membrane from the PDMS mold containing the channel. In most cases, the composite materials remain attached within the mold. The fabricated materials are rigid enough to be handled using precise tweezers. We then stamped the composite materials on a metallic mount covered by a conductive tape. Microscopic images were obtained using a tabletop SEM (Hitachi TM3030).

To obtain the SEM pictures of the transverse sections of the composite materials, see Figure 10, we proceeded as follows. We first made an incision with a sharp blade within the PDMS block containing the channels, transversally to the microchannels (see Figure 1). The depth of this straight incision across the device is small enough (3–4 mm) to prevent from the damage of the composite materials. The whole PDMS chip is then immersed in liquid nitrogen for about 1–2 min. After removal, the chip turned brittle and we manually broke the device following the initial incision. This procedure does not deform the materials within the chip. SEM images of the transverse dimensions of the materials are then obtained using a SEM pin mounted on a tilt/rotate stage. This stage makes it possible to align each cross-section with the SEM detector in order to get quantitative measurements of their dimensions.

4 Results

4.1 Growth dynamics

A typical experiment is shown in Figure 1b for the case $\phi_0 = 0.018$, $\psi_0 = 0.0003$ (mass fraction), $h \times w = 25 \times 150$ μm^2 and $L_0 = 7.5$ mm. Using eq 10, we estimated the local absorbance $A(X,T)$ along the channel from such images, and thus the relative values of the CNT concentration field $\psi(X,T)$. Such an analysis leads to the space-time plot shown Figure 6. This space-time

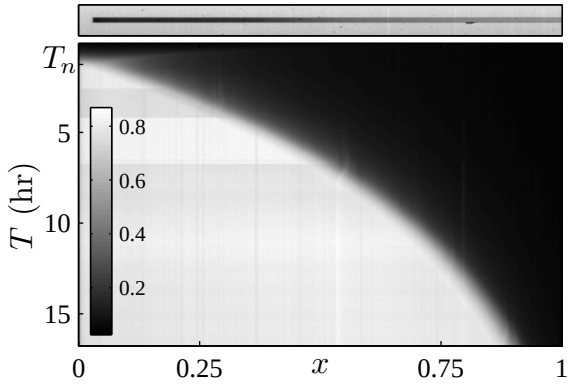

Fig. 6 Top: typical snapshot of a given channel at a given time of the concentration process (channel width $w = 150$ μm). Bottom: space-time plot of the absorbance estimated using eq 10 on a series of images as the one displayed above. Positions x within the channel are rescaled by $L_0 = 7.5$ mm.

plot displays obvious similarities with the theoretical dynamics expected for the polymer concentration field, see Figure 3b.

At early stages for $T < T_n \approx 70$–80 min, CNT continuously concentrate within the channel. For $T > T_n$, we observed the *nucleation* at the tip of the channel of a plateau of $A \approx 0.8$, which then invades the channel. This corresponds to the growth of the polymeric material within the channel. This space-time plot also reveals that the growth rate of the material significantly slows down along the channel. Note that $A \approx 0.8$ corresponds to the saturation of the measurements (see section 3), and the position of the solid material cannot *a priori* be dectected precisely from these data.

Figure 7 displays some absorbance profiles to better evidence the dynamics before and after T_n. Figure 7a focuses on the con-

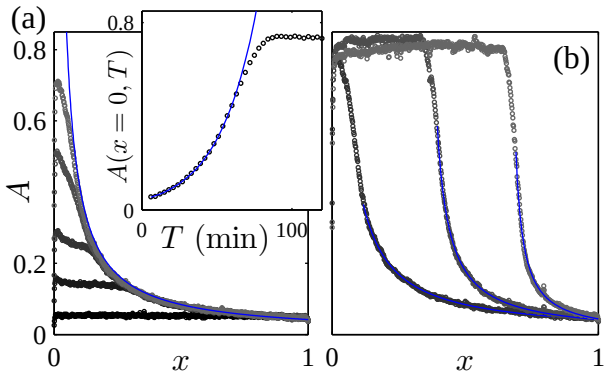

Fig. 7 (a) Absorbance profiles before the growth of the material at $T = 6$, 33, 48, 63 and 78 min (from black to gray dots). The blue curve corresponds to the hyperbolic profile $A = A_0 L_0 / X$. Inset: absorbance at the tip of the channel vs. time T. The blue curve is an exponential fit. (b) Absorbance profiles during the progression of the dense material along the channel at $T = 90$, 300, and 600 min (from black to gray dots). The blue curves are shifted hyperbolic profiles given by eq 11.

centration profiles for $T < T_n \approx 70$–80 min, i.e. before the growth of the solid material. These profiles are in excellent agreement with the theoretical predictions given by eq 6, see for instance the buildup of the hyperbolic profile displayed in blue, and the exponential increase of the concentration at the tip of the channel (see inset of Figure 7a). This regime is thus consistent with the one described by eq 6 corresponding to the transport dominated by convection in a dilute solution, i.e. $\phi(x)v(x) \approx \phi_0 v(x=1)$, with $v(x) = -x$, see section 2.

Importantly, these data also make possible the *in-situ* calibration of the pervaporation rate q_e. Indeed, the exponential increase of the concentration yields an estimate of the time scale $\tau_e = (hw)/q_e$, see eq 6 which becomes $\phi(x, t=0) = \phi_0 \exp((1-h_e)t)$ for $h_e \neq 0$. The good agreement with the theoretical model also demonstrates that our estimates of the CNT concentration using eq 10 are valid, and more importantly that the concentration field of the CNT follows the concentration field of PVA, as claimed above.

Figure 7b show typical profiles during the growth of the composite material within the channel. As discussed above, the saturation of A prevents us from estimating precisely the exact position of the advancing front. Nevertheless, the concentration

profiles upstream the advancing front are well-fitted by *shifted* hyperbolic profiles

$$A(x,t) = A_0 \frac{1-x_f}{x-x_f}, \qquad (11)$$

see the blue lines in Figure 7, where x_f is the only free parameter and $A_0 \approx 0.042$ corresponds to the fixed absorbance at $x = 1$. It again shows that the transport is dominated by convection for $x > x_f$, see eq 7 in section 2

The fitted values of x_f yield estimates of the positions of the front. Note that for the case shown Figure 7, we can estimate the concentration of PVA just below the saturation value $A \approx 0.8$ by $\phi = (0.8/A_0)\phi_0 \approx 0.35$. This value is smaller than $\phi \approx 1$ expected for a dry composite, indicating our setup cannot fully cover the concentration range ≈ 0.35–1. Nevertheless, the estimates of the dry front positions x_f using eq (11) are very close to the x positions at which A begins to saturate owing to the strong divergence of the hyperbolic profile near x_f (see for instance the theoretical case displayed Fig. 4b). In other words, the concentration range 0.35–1 is expected to be observed only on a very small scale within the channel.

This value is smaller than the one expected for a dry composite $\phi \approx 1$. However, the strong divergence of the hyperbolic profile suggests that the concentration reaches $\phi \approx 1$ at a position which is very close to the extent of the plateau of saturation.

Figure 8a reports measurements of X_f vt. T obtained for various L_0 ($L_0 = 5$–15 mm) and for the same transverse dimensions as above. X_f corresponds to a very good approximation to the position of the growing material, and this plot evidences again the slowing down of the growth rate along the channel. The inset of Figure 8a also shows the rescaling of the dynamics with the natural variables of the process, L_0 and τ_e. The perfect collapse of the data underlines the excellent control provided by the microfluidic geometry. It also strongly suggests that transport equations such as eqs 3 and 4, are expected to describe quantitatively this dynamics. This is indeed confirmed by the perfect fit of this dynamics by the exponential decay eq 8, derived theoretically in section 2. Such a fit yields both the *induction* time τ_n and the characteristic time τ_g of the growth of the material within the channel.

To go a step further into the comparison with the theoretical predictions, we screened different initial polymer concentrations ϕ_0 using the same dimensions $h \times w = 25 \times 90\ \mu\text{m}^2$ and $L_0 = 5$ mm. In Figure 8(b), we reported the estimated τ_g and τ_n from these screening measurements. We first observed that $\tau_g = 0.5/\phi_0$ over the wide range of concentrations investigated. The induction times display two different regimes. For $\phi_0 > 0.01$, τ_n slightly decreases from 4.6 to 2.1, see the solid curve indicating the logarithmic decrease $\tau_n \sim -\log(\phi_0)$. For $\phi_0 < 0.01$, τ_n shows a pronounced increase with the decreasing concentrations up to ≈ 30 for $\phi_0 \approx 0.001$. This behavior is consistent with our theoretical

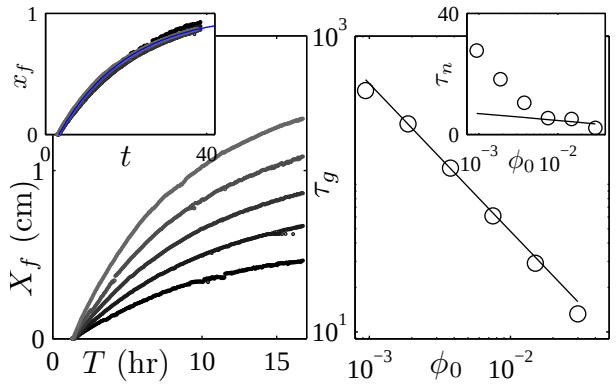

Fig. 8 (a): Growth dynamics for several $L_0 = 5$–15 mm (from black to gray dots) and for $h \times w = 25 \times 150\ \mu\text{m}^2$. Inset: rescaling of the data x_f vs. t. The blue line is an exponential fit by eq (8). (b) Fitted values τ_g vs. ϕ_0 ($h \times w = 25 \times 90\ \mu\text{m}^2$ and $L_0 = 5$ mm). The solid line is $\tau_g = 0.5/\phi_0$. Inset: corresponding τ_n vs. ϕ_0, the solid line is $\tau_n = -\log(\phi_0)$.

predictions, see the inset of Figure 5b, and with the same crossover value $\phi_0 \approx 0.01$ indicating therefore that $\text{Pe} \approx 10^4$ in our experiments as expected.

All the above observations are in excellent agreement with our theoretical predictions. However, the matching is only qualitative as we observed experimentally $\tau_g \approx 0.5/\phi_0$, see Figure 8, whereas theoretical arguments based on conservation of solutes predict strictly $\tau_g \approx 1/\phi_0$. This deviation would suggest that the concentration within the growing material is $\phi \approx 0.5$. Note that such a huge discrepancy cannot be explained by the assumption $h_e = 0$ in the above numerical resolution of eqs 3 and 4. Indeed, humidities h_e ranges experimentally between $h_e = 0.2$–0.4. We thus expect that the concentration of the material at equilibrium with such values is very close to $\phi \approx 1$, as $\phi > 0.97$ for $a(\phi) < 0.4$, see Figure 3a.

We report below experiments which reveal that this discrepancy comes from the deformation on the PDMS matrix during the growth of the materials.

4.2 Failure of the quantitative description: deformations of the channels and thermo-mechanical properties of the polymer

We first report a rough screening experiment ($\phi_0 = 0.008$) obtained using a chip with 5 pervaporators with $L_0 = 16$ mm, $h = 25\ \mu$m, and w from 100 to 500 μm, see Figure 9a. As above, the exponential increase of the CNT concentration at the tips of the channels makes possible the calibration of τ_e, which vary from 1300 to 1600 s. After a transient, we observed the growth of materials within the channels and Figure 9a shows the corresponding rescaled dynamics x_f vs. t. The curves do not collapse at all, even if they share a common induction time $\tau_n \approx 2.5$. All these

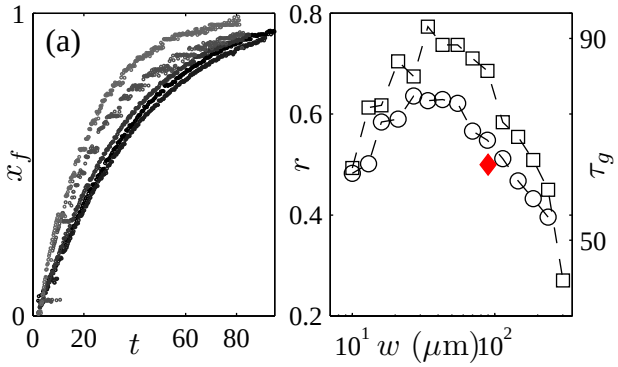

Fig. 9 (a) Rescaled growth of the materials investigated for the case $\phi_0 = 0.008$, $L_0 = 16$ mm, $h = 25$ μm and w ranging from 100 to 500 μm (from black to gray dots). (b) τ_g vs. w (square) and shrinkage ratio r vs. w ($\circ$, see text) for the case $\phi_0 = 0.006$, $L_0 = 5$ mm, $h = 25$ μm. r were estimated using SEM images of the transverse dimensions of the dried materials, see Figure 10. The red diamond comes from the independant measurements τ_g vs. ϕ_0 shown Figure 8b, see text.

curves are correctly fitted by the exponential decay described by eq 8 (not shown) but the growth rate for the smallest width is significantly smaller than the one for the largest w.

To cover a wider range of aspect ratios h/w and evaporation times τ_e, we used a screening chip with 15 pervaporators with $L_0 = 5$ mm, $h = 25$ μm and w ranging logarithmically from 10 to 300 μm. For this chip, τ_e ranges from 200 to 1200 s, and Pe from $\approx 10^2$ to $\approx 10^3$. We estimated as done previously the time scales τ_g from the growth dynamics x_f vs. t ($\phi_0 = 0.006$). The corresponding data are displayed Figure 9b and again the growth depends on the channel width w. Surprisingly, this wider screening now reveals a non-monotonic behavior: τ_g first increases up to 90 for $w = 50$ μm, then decreases down to 40 for the largest width (300 μm). This striking result evidences that our approach based on conservation equations misses an ingredient.

The images obtained using our stereomicroscope on a wide field of view (see section 3 and Figure 1b) prevent us to observe precisely the solification front. However, images obtained at a higher spatial resolution using a microscope clearly show that the channels deform significantly close to the advancing front x_f (see SI for the corresponding images). To get more insight into this observation, we measured systematically the transverse dimensions of materials obtained within the channels.

Figure 10 shows some SEM images of the transverse sections of the materials within the chip, see section 3 for the experimental details. The images taken at high resolution show clearly that the materials do not fill entirely the PDMS channel section $h \times w$. For large width w, the top faces of the materials are even curved suggesting that the slight deflection of the PDMS membrane for these large w impacts the final shapes of the materials. For $w <$

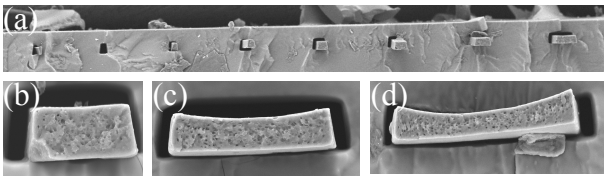

Fig. 10 (a) Wide SEM view of the sections of the materials embedded within the PDMS chip (see section 3 for the experimental details leading to such images). From left to right, the width of the channels are $w = 10$, 13, 16, 21, 27, 34, 43, and 55 μm. (b) to (d): SEM images at a higher resolution for $w = 43$, 90, and 145 μm.

50 μm the transerve cross-sections of the micro-material are more rectangular but always significantly smaller than $h \times w$. These SEM observations demonstrate without ambiguity that the PDMS matrix significantly deform during the solidification process, as previously reported for the case of cellulose acetate solutions[15].

To go a step further, we estimated the skrinkage ratio $r = S/(hw)$, where S is the cross-sections of the materials obtained by analysing the SEM images. Figure 9b reports the estimated r vs. w, together with τ_g vs. w for the same experiment using the chip screening logarithmically w from 10 to 300 μm. This plot shows the same non-monotonic behavior for the skrinkage ratio: r first increases from 0.5 to 0.6 for $w = 50$ μm, then decreases down to 0.4 for the largest w. These two bell-shaped curves suggest that the deformations of the PDMS matrix may explain the non-rescaling of x_f vs. t, but also the experimental scaling $\tau_g \approx 0.5/\phi_0$ which differs from the expected theoretical one $\tau_g = 1/\phi_0$.

Indeed, our above one-dimensional theoretical description only applies for a channel with a constant geometry $h \times w$. Strong arguments based on solutes conservation lead to eq 9 which does not *quantitatively* predict the observed growth rates. If we now assume that the channel cross-section varies from $h \times w$ to $\approx S$ at the solidification front x_f, eq 9 becomes

$$r\dot{x}_f = \phi_0(1 - x_f), \tag{12}$$

to take into account the shrinkage of the channel in the conservation of the solute. This last equation predicts an exponential decay as in eq 8 but with $\tau_g = r/\phi_0$. This explains the bell-shaped curve τ_g vs. w reported Figure 9b which follows the curve r vs. w. Moreover, our screening experiments, see Figure 8b, yield $\tau_g \approx 0.5/\phi_0$ for $h \times w = 25 \times 90$ μm^2. This value reported in Figure 9b is consistent with the shrinkage ratio measured *independently* for the same geometry. This strongly supports that the quantitative mismatch and the bell-shape curve τ_g vs. w displayed Figure 9b are both explained by the shrinkage of the material during the solidification.

The deformations of the PDMS matrix at the solidification front result from intricate phenomena coupling the adhesion forces of

the PVA/solution on the PDMS walls and the strong increase of the visco-elastic coefficients of the polymer mixture when the latter becomes glassy when $\phi \to 1$ [25,26]. In this latter case, water is expected to permeate through a glassy crust at a very low rate owing to the strong decrease of the collective diffusion coefficient at high concentrations [21]. In this regime, our above description of the growth based on a one dimensional uniform permeation mechanism would fail as $D < q_e$ [19]. Nevertheless, these subtle effects occur only in a narrow region upstream the growing front (on a length scale $\sim L_0/\sqrt{\mathrm{Pe}}$) as transport is dominated by convection in our experimental case. Therefore, our description of the growth dynamics based on general conservation equations is not affected by these effects which are taken into account phenomenologically through the skrinkage ratio r.

5 Conclusions

We investigated in depth using both theory and experiments, the dynamics of concentration of polymer solutions by microfluidic pervaporation, up to the formation of a polymer material within the micromold. Our experimental approach which makes an extensive use of the screening opportunities offered by the microfluidic tools, reveal that the key ingredients of the growth (induction time and growth time) are simply captured by a simple model based on transport equations. We also demonstrated that the process is dominated by convection and that the specific shape of the chemical activity $a(\phi)$ is not a crucial parameter. The guidelines derived experimentally and theoretically above are thus general and can apply to other polymer solutions in similar conditions.

The only *semi-quantitative* mismatch between the theoretical predictions and the experiments comes from the deformation of the matrix during the solidification. This problem is certainly related to the strongly increasing viscosity of the polymer solution at high concentrations [33] as suggested by Demko *et al.* [15]. Nevertheless, other factors are expected to play a significant role. In particular, adhesion and the strong increase of the elastic forces of the solidifying polymer within the channel when the latter crosses the glass transition [25,26]. The full description of the forces exerted by the drying polymer solution should also take into account both the average flow of the solution at a rate $v(x)$ in the channel and the relative polymer/solvant flow induced by pervaporation [34–36]. More specifically, the bell-shape curve r vs. w observed in our work also reveals that the mechanical deformations of the matrix depend strongly of the aspect ratio h/w. Importantly, our measurements suggest that there exists an optimum $w/h \sim 1$–2 minimizing the shrinkage of the material.

To conclude, our study demonstrates for the first time the excellent control imparted by the microfluidic geometry on the fabrication of composite materials with well-defined shapes. This approach only requires dilute inks (colloidal charges in a polymer solution), avoiding the need for thermal of UV- post treatments as in the seminal MIMIC procedure (micromoulding in capillaries) [13,14]. We will soon report a complete investigation of the possibilities offered by this technique to make micro-materials which may have applications as MEMS [17,18].

Acknowledgments

We thank J. Leng and I. Ly for useful discussions. We also thank Solvay and CNRS for fundings. The research leading to these results received fundings from *Région Aquitaine* for the grant *MEMS ORGA*. This work was also supported by the LabEx AMADEus (ANR-10-LABX-42) in the framework of IdEx Bordeaux (ANR-10-IDEX-03-02) i.e. the Investissements d'Avenir programme of the French government managed by the Agence Nationale de la Recherche

References

1 E. Verneuil, A. Buguin and P. Silberzan, *Europhys. Lett.*, 2004, **68**, 412–418.
2 G. C. Randall and P. S. Doyle, *Proc. Natl. Acad. Sci. USA*, 2005, **102**, 10813–10818.
3 M. T. Demko, J. C. Cheng and A. P. Pisano, *Langmuir*, 2010, **26**, 16710–16714.
4 A. Merlin, J.-B. Salmon and J. Leng, *Soft Matter*, 2012, **8**, 3526–3537.
5 J. Angly, A. Iazzolino, J.-B. Salmon, J. Leng, S. Chandran, V. Ponsinet, A. Desert, A. L. Beulze, S. Mornet, M. Treguer-Delapierre and M. Correa-Duarte, *ACS Nano*, 2013, **7**, 6465–6477.
6 J. Leng, B. Lonetti, P. Tabeling, M. Joanicot and A. Ajdari, *Phys. Rev. Lett.*, 2006, **96**, 084503–084506.
7 J. Leng, M. Joanicot and A. Ajdari, *Langmuir*, 2007, **23**, 2315–2317.
8 L. Daubersies, J. Leng and J.-B. Salmon, *Lab chip*, 2013, **13**, 910–919.
9 N. Ziane, M. Guirardel, J. Leng and J.-B. Salmon, *Soft Matter*, 2015, **11**, 3637–3642.
10 P. Calvert, *Chem. Mater.*, 2001, **13**, 3299–3305.
11 P. Tseng, C. Murray, D. Kim and D. DiCarlo, *Lab Chip*, 2014, **7**, 1491–1495.
12 Y. Xia and G. M. Whitesides, *Annual Review of Materials Science*, 1998, **28**, 153–184.
13 E. Kim, Y. Xia and G. M. Whitesides, *Nature*, 1995, **375**, 581–583.
14 E. Kim, Y. Xia and G. M. Whitesides, *J. Am. Chem. Soc.*, 1996, **118**, 5731–5722.
15 M. T. Demko, J. C. Cheng and A. P. Pisano, *Langmuir*, 2012, **28**, 9857–9863.
16 M. T. Demko, J. C. Cheng and A. P. Pisano, *ACS Nano*, 2012, **6**, 6890–6896.

17 I. Kang, M. J. Schulz, J. H. Kim, V. Shanov and D. Shi, *Smart Mater. Struct.*, 2006, **15**, 737–748.

18 D. J. Lipomi, M. Vosgueritchian, B. C.-K. Tee, S. L. Hellstrom, J. A. Lee, C. H. Fox and Z. Bao, *Nature nanotechnology*, 2011, **6**, 788–792.

19 M. Schindler and A. Ajdari, *Eur. Phys. J E*, 2009, **28**, 27–45.

20 I. Teraoka, *Polymer Solutions: An Introduction to Physical Properties*, Wiley, 2002.

21 S. Jeck, P. Scharfer, W. Schabel and M. Kind, *Chemical Engineering and Processing*, 2011, **50**, 543–550.

22 *Handbook Of Size Exclusion Chromatography And Related Techniques: Revised And Expanded*, ed. C. Wu, CRC Press, 2003.

23 P. Miaudet, S. Badaire, A. Derré, M. Maugey, V. Pichot, P. Launois, P. Poulin and C. Zakri, *Nanoletters*, 2005, **5**, 2212–2215.

24 C. Bartholome, A. Derré, O. Roubeau, C. Zakri and P. Poulin, *Nanotechnology*, 2008, **19**, 1–6.

25 J. S. Park, J. W. Park and E. Ruckenstein, *Journal of Applied Polymer Science*, 2001, **82**, 1816.

26 P. Miaudet, A. Derré, M. Maugey, C. Zakri, P. Piccione, R. Inoubli and P. Poulin, *Science*, 2007, **318**, 5854.

27 C. Mercader, V. Denis-Lutard, S. Jestin, M. Maugey, A. Derré, C. Zakri and P. Poulin, *Journal of Applied Polymer Science*, 2012, **125**, 191–196.

28 E. L. Cussler, *Diffusion : Mass Transfer in Fluid Systems*, Cambridge University Press, 1997.

29 B. R. Bird, E. W. Stewart and E. N. Lightfoot, *Transport phenomena*, Wiley international edition, 2002.

30 W. B. Russel, D. A. Saville and W. R. Schowalter, *Colloidal dispersions*, Cambridge University Press, 1989.

31 X. Noblin, L. Mahadevan, I. A. Coomaraswamy, D. A. Weitz, N. M. Holbrook and M. A. Zwieniecki, *Proc. Natl. Acad. Sci. U. S. A*, 2008, **105**, 9140–9144.

32 K. Saint-Aubin, P. Poulin, H. Saadaoui, M. Maugey and C. Zakri, *Langmuir*, 2009, **25**, 13206–13211.

33 M. Bercea, S. Morariu and D. Rusu, *Soft Matter*, 2013, **9**, 1244–1253.

34 M. Doi and A. Onuki, *J. Phys. II France*, 1992, **2**, 1631–1656.

35 T. Okuzono, K. Ozawa and M. Doi, *Phys. Rev. Lett.*, 2006, **97**, 136103–136106.

36 T. Okuzono and M. Doi, *Phys. Rev. E*, 2008, **77**, 030501–030504.